Zentrum für Technomathematik
Fachbereich 3 – Mathematik und Informatik

Stochastic model and simulation of mechanical responses for texturized microscale materials under elastic deformation

Pavel Bobrov   Jonathan Montalvo Urquizo
Alfred Schmidt   Werner Wosniok

Report 10–04

Stochastic model and simulation of mechanical responses for texturized microscale materials under elastic deformation

P. Bobrov[a,*], J. Montalvo-Urquizo[b,*], A. Schmidt[b], W. Wosniok[a]

[a]*Institut für Statistik, Fachbereich 3, University of Bremen, Germany*
[b]*Zentrum für Technomathematik, Fachbereich 3, University of Bremen, Germany*

Abstract

A stochastic model for the elastic tensor components of a texturized material is presented. The model produces the distributions of the stiffness matrix components for single grains, as a result of the preferred directions given by the material texture.

Based on the resulting distributions, we simulate the responses of a representative volume element under different loading modes. The simulation of the responses uses a FEM solver for the elasticity problem and includes the anisotropies due to the material's texture as well as the ones arising from the slightly different orientation of the different crystals.

With this method, the distributions of the strain and stress tensors components can be obtained in practice by only knowing the texture of the material. Specific examples of computed distributions for texturized Aluminium will be shown, together with the resulting distributions of the FEM-calulated mechanical responses of a polycrystal.

1. Introduction

Within the production of metallic micro-components, modelling of the single grains composing the material pieces becomes important, as the local

---

[*]Corresponding author

Email addresses: `bobrov@math.uni-bremen.de` (P. Bobrov),
`montalvo@math.uni-bremen.de` (J. Montalvo-Urquizo), `schmidt@math.uni-bremen.de`
(A. Schmidt), `wwosniok@math.uni-bremen.de` (W. Wosniok)

differences between them cannot be assumed to be small when compared to the sizes of the complete work pieces.

In the case of texturized material, it is well known that all the grains have a preferred orientation, but the actual orientation of a single crystal cannot be determined a-priori. These uncertainties are here handled using a stochastic model for the construction of the elastic moduli of the single crystals.

While considering a two-scale modelling of the microcomponents, the "micro" scale corresponds to a small material piece holding some grains of the texturized material. The material response in the "macro" scale (the complete piece, which is also of small dimension) will be strongly determined by the anisotropic responses in the microscale. The importance of the microscale responses motivate this work, where we model the elastic components of monocrystals stochastically and generate the FEM-simulated responses of a representative volume element (RVE) of material.

The resulting responses on the microscale can later be used in a two-scale simulation, in which usually the computation of a large number of micro-problems slows the whole simulation process. The microscale responses presented here can be used as a module for computing a good approximation to the solution in each micro-problem using a neglectible amount of computation time.

Section 2 presents the stochastic model for the monocrystals, together with some examples of the resulting distributions for the stiffness matrix components. Section 3 describes the simulation strategy for creating a randomized geometry of a polycrystal RVE and presents the resulting distributions of stresses obtained for the different load modes of the RVE. Finally, Section 4 presents a an example of two-scale simulation.

2. Stochastic model for the crystals in the texturized material

2.1. The problem

The elastic properties of a polycrystallite material are described by the compliance tensor S_{ijkl} or the stiffness tensor C_{ijkl} $(i, j, k, l = 1, 2, 3)$, [1, 2]. Because of the symmetry of strain and stress tensor, and for energetical considerations both tensors can be expressed by symmetric matrices S_{ij} and C_{ij} $(i, j = 1, 2, ..., 6)$, respectively, each containing 21 independent components. In the sequel we focus on the compliance tensor, the components of which are termed elastic moduli.

2

For anisotropic crystals the symmetry properties of the various crystal systems reduce the number of independent matrix elements [1]. As an example, there are only three independent elements for a cubic crystal system.

To describe a single crystal, an orthogonal coordinate system tightly connected to the crystal axes may be chosen. Such a system is called a crystal physical coordinate system. We choose the directions of the cube edges as axes for a cubic crystal system. In this coordinate system the compliance tensor may be represented in matrix form as

$$\begin{pmatrix} s_{11} & s_{12} & s_{12} & 0 & 0 & 0 \\ & s_{11} & s_{12} & 0 & 0 & 0 \\ & & s_{11} & 0 & 0 & 0 \\ & & & s_{44} & 0 & 0 \\ & \text{sym} & & & s_{44} & 0 \\ & & & & & s_{44} \end{pmatrix} \tag{1}$$

where $s_{11} = s_{1111}$, $s_{12} = s_{1122}$ and $s_{44} = s_{1212}$.

Now we define an orthogonal coordinate system in the specimen. This coordinate system may be chosen arbitrarily. We use the RTN (Rolling, Transversal, Normal) system, which is commonly used for sheets and foils. We describe the orientation of a crystallite in a polycrystal by a rotation g, which maps the global reference system on the crystal physical system. These rotations constitute the rotation group SO(3). For the tensor S_{ijkl} in the RTN system we have the tensor representation of the rotation group

$$S_{ijkl} = g_{ip}g_{jq}g_{km}g_{ln}s_{pqmn} \tag{2}$$

where g_{ij} denotes the components of the rotation matrix and components with repeated indices are added.

As crystallites in the polycrystal are randomly orientated, also the components g_{ij} show a random variation, which induces random variations in the values of the elastic moduli. If the orientations of the crystallites are uniformly distributed, the corresponding polycrystal is quasi isotropic, and if a principal orientation exists, we have a texture.

Here, we consider the distributions of the matrix elements of the compliance tensor for a polycrystal that are induced by normal measures on SO(3).

2.2. Distributions on SO(3)

We consider distributions $d\mu = f(g)dg$, $g \in$ SO(3), where dg is an invariant measure on SO(3). Parametrising the rotation g by Euler angles

3

$g = g(\varphi_1, \theta, \varphi_2)$, $\theta \in [0, \pi]$, and $\varphi_1, \varphi_2 \in [-\pi, \pi)$ we have

$$dg = \frac{\sin \theta d\theta}{2} \frac{d\varphi_1}{2\pi} \frac{d\varphi_2}{2\pi}. \tag{3}$$

The texture function $f(g)$ depends on the orientation [3], and may be expanded as a series of generalized spheric functions

$$f(g) = \sum_{l=0}^{\infty} \sum_{m,n=-l}^{l} C_{mn}^l T_{mn}^l(g), \tag{4}$$

and if the polycrystal is quasi isotropic, then $f(g) = 1$.

An important distribution class on SO(3) is the class of normal distributions. We define these according to [4, 5] in the following way: a measure μ on SO(3) has a normal distribution, if μ is infinitely divisible and not idempotent, and if for each irreducible representation T_g of the group holds that

$$\int_G T_g d\mu(g) = \exp\left[\sum_{i,j} \alpha_{ij} A_i A_j + \sum_i \alpha_i A_i \right], \tag{5}$$

where A_i are infinitesimal operators of this representation, (α_{ij}) is a positive definite symmetric matrix, and α_i are real numbers. If $\alpha_{ij} = 0$ for $i \neq j$, we have a canonical normal distribution [6] with analytical probability distribution

$$f(g) = \sum_{l=0}^{\infty} (2l+1) \exp[-l(l+1)p^2] \times$$
$$\times \sum_{m=-l}^{l} \exp[m^2(q^2 - r^2)] \exp[-im(\varphi_1 + \varphi_2)] P_{mm}^l(\cos \theta). \tag{6}$$

Here, $P_{mm}^l(x)$ are Jacobian polynomials with parameters q, r, p and, although we consider orientation distributions belonging to the family of canonical distributions, equation (6) is not useful for our purpose.

Another way to derive the desired distributions lies in the application of Parthasarathy's central limit theorem for the rotation group [5]. We need some additional notation for this theorem. Let $g_n = \int_{\text{SO}(3)} g d\mu_n(g)$ be the mean of the measure $\mu_n(g)$ for $n = 1, 2, 3, \ldots, \mu_n^{*n}$ with $d\mu_2^{*2}(g) = \int_{\text{SO}(3)} \mu_2(gg_1^{-1}) d\mu_2(g_1)$, μ_n denotes the n-fold convolution and $\mu_n(SO(3) \backslash U_e)$ is the value of the measure $\mu_n(g)$ outside the neighbourhood U_e of the zero element e of the group.

Parthasarathy's Central Limit Theorem (CLT) for SO(3) states that for a given sequence $\{\mu_n\}$, $n = 1, 2, 3, \ldots$ of distributions on SO(3), which converges to a degenerate distribution in e as $n \to \infty$, the sequence of convolutions μ_n^{*n} converges to a normal distribution if and only if for $n \to \infty$ holds

1. $n(1 - |g_n|) < \infty$
2. $n\mu_n(SO(3)\backslash U_e) \to 0$

Further, if additionally holds that $\lim\limits_{n\to\infty} n(e - g_n) = A$, then the parameters α_{ij} and α_i of the distribution μ_n^{*n} are given by

$$-A = \sum_{i=1}^{3}\sum_{j=1}^{3}\alpha_{ij}a_i a_j + \sum_{i=1}^{3}\alpha_i a_i \tag{7}$$

with $a_i = \lim\limits_{t\to 0}\frac{g_i(t)-e}{t}$, where $g_i(t)$ are the one-parametric subgroups of SO(3).

2.3. Simulation of orientation distributions

Due to the CLT we may specify an order $\mu_n(g)$. We use the concept of small rotations [7] for this purpose. The set of small rotations corresponds to a certain set of Euler angles of the form

$$\begin{cases} 1 - (e_z', e_z) = 1 - \cos\theta \leq a \\ 1 - (e_x', e_x) = 1 - \cos\varphi_1\cos\varphi_2 + \sin\varphi_1\sin\varphi_2\cos\theta \leq b \\ 1 - (e_y', e_y) = 1 + \sin\varphi_1\sin\varphi_2 - \cos\varphi_1\cos\varphi_2\cos\theta \leq b \\ 0 \leq a, b \ll 1 \end{cases} \tag{8}$$

Here, (e_x, e_y, e_z) form a basis before a small rotation and (e_x', e_y', e_z') therafter. Given that $a, b \ll 1$, Equation (8) simplifies to

$$\frac{\theta^2}{2} \leq a \ , \ \frac{(\varphi_1 + \varphi_2)^2}{2} \leq b. \tag{9}$$

and the set of small rotations now is represented by the region

$$\Pi(a, b) = \left\{(\varphi_1, \theta, \varphi_2): \ \theta \leq \sqrt{2a} = \bar{a} \ , \ |\varphi_1 + \varphi_2| \leq \sqrt{2b} = \bar{b}\right\} \tag{10}$$

The sequence of measures $d\mu_n = f_n(g)dg$, with dg denoting the invariant measure, f_n the rectangular distribution in $\Pi(a_n, b_n)$, $a_n = \bar{a}/\sqrt{n}$, $b_n = \bar{b}/\sqrt{n}$ and

$$f_n(\varphi_1, \theta, \varphi_2) = \begin{cases} \frac{2}{1-\cos a_n} \cdot \frac{4\pi^2}{b_n(4\pi - b_n)} & (\varphi_1, \theta, \varphi_2) \in \Pi(a_n, b_n) \\ 0 & (\varphi_1, \theta, \varphi_2) \notin \Pi(a_n, b_n) \end{cases} \tag{11}$$

corresponds to the sequence of convolutions

$$d\mu_n^{*n} = \left[\int\limits_{SO(3)} dg_{n-1} f_n(gg_{n-1}^{-1})... \int\limits_{SO(3)} dg_1 f_n(g_2 g_1^{-1}) f_n(g_1) \right] dg , \qquad (12)$$

which according to [7] converges for $t \to \infty$ to the canonical normal distribution on SO(3) with parameters $q^2 = \bar{a}^2/8$ and $r^2 = \bar{b}^2/6$.

The realisation of the random variable $g \in$SO(3) with distribution (12) is the product of the small random rotations $g = g_1 g_2...g_n$, where $g_i = g(\varphi_1^i, \theta^i, \varphi_2^i) \in$SO(3) with density (11). The Euler angles $(\varphi_1^i, \theta^i, \varphi_2^i)$ are given by [7]:

$$\varphi_1^i = \begin{cases} -(\pi + b_n) + \sqrt{b_n^2 + 2b_n(4\pi - b_n)\xi_1^i} ; & \xi_1^i < \frac{3b_n}{2(4\pi - b_n)} \\[2ex] \left(\frac{b_n}{4} - \pi\right) + \frac{4\pi - b_n}{2}\xi_1^i ; & \frac{3b_n}{2(4\pi - b_n)} \leq \xi_1^i < 1 - \frac{3b_n}{2(4\pi - b_n)} \\[2ex] (\pi + b_n) - \sqrt{b_n^2 + 2b_n(4\pi - b_n)(1 - \xi_1^i)} ; & 1 - \frac{3b_n}{2(4\pi - b_n)} \leq \xi_1^i \end{cases}$$

$$\theta^i = \arccos\left(1 - \xi_2^i(1 - \cos a_n)\right)$$

$$\varphi_2^i = \begin{cases} \pi - \xi_3^i(b_n + \pi + \varphi_1^i) ; & -\pi \leq \varphi_1^i < b_n - \pi \\[2ex] -\varphi_1^i + 2b_n\left(\xi_3^i - \frac{1}{2}\right) ; & |\varphi_1^i| \leq \pi - b_n \\[2ex] -\pi + \xi_3^i(b_n + \pi - \varphi_1^i) ; & \pi - b_n < \varphi_1^i \leq \pi \end{cases}$$

$$(13)$$

where ξ_1^i, ξ_2^i, ξ_3^i are independent and uniformly distributed in [0,1].

In [7], it was shown that convolution parameters $n \geq 20$ generate a good agreement of μ_n^{*n} with a normal distribution with density as in equation (6).

The distribution of crystallite orientations may be modelled by Monte Carlo simulation and the material parameters of interest are subsequently derived from these.

With θ denoting the nutation angle on the sphere, Figure 1 shows the histogram for the distribution of the nutation angle projection obtained after 10000 realisations for the values of $\bar{a} = 0.2$, $\bar{b} = 0.5$ and $n = 50$.

For the case of polycrystal material having a texture g_0 with main orientation different from the cube coordinate edges, the resulting normal distri-

6
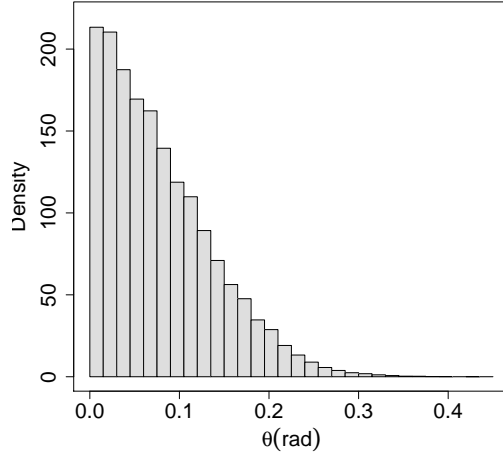
Figure 1: Histogram of the nutation angle distribution for $\bar{a} = 0.2$, $\bar{b} = 0.5$ and $n = 50$.

bution (in the sense of SO(3)) for the nutation angle is shifted towards this actual orientation.

2.4. Results for the elastic mouli

Equation (2) leads to the tensor (1) in the form

$$S_{11} = s_{11} - 2\mu^s \left(g_{11}^2 g_{21}^2 + g_{11}^2 g_{31}^2 + g_{21}^2 g_{31}^2 \right)$$

$$S_{12} = s_{12} + \mu^s \left(g_{11}^2 g_{12}^2 + g_{21}^2 g_{22}^2 + g_{31}^2 g_{32}^2 \right)$$

$$S_{44} = s_{44} + 4\mu^s \left(g_{12}^2 g_{13}^2 + g_{22}^2 g_{23}^2 + g_{32}^2 g_{33}^2 \right) \tag{14}$$

$$S_{14} = 2\mu^s (g_{11}^2 g_{12} g_{13} + g_{21}^2 g_{22} g_{23} + g_{31}^2 g_{32} g_{33})$$

$$S_{16} = 2\mu^s (g_{11}^3 g_{12} + g_{21}^3 g_{22} + g_{31}^3 g_{32})$$

where $\mu^s = s_{11} - s_{12} - s_{44}/2$ is the measure of anisotropy and all other S_{ij} can be obtained from cyclical re-arrangement of indices, e.g. $S_{66} = s_{44} + 4\mu^s \left(g_{11}^2 g_{12}^2 + g_{21}^2 g_{22}^2 + g_{31}^2 g_{32}^2 \right).$

7
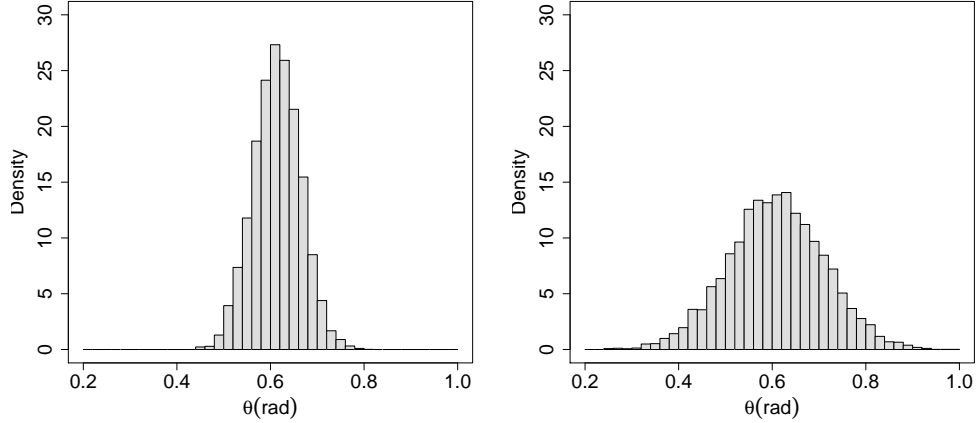
Figure 2: Histograms of the nutation angle distributions given a RTN texture. Left: $\bar{a} = 0.1$, $\bar{b} = 0.2$; Right: $\bar{a} = 0.2$, $\bar{b} = 0.4$ and $n = 100$.

If the elements of the rotation matrix g_{ij} are parametrized by Euler angles, the equations (14) may be written as

$$S_{ij} = s_{ij} + \mu^s C_{ij} \Lambda_{ij}(\varphi_1, \theta, \varphi_2).$$

Here, we have a normal distribution of $g = g(\varphi_1, \theta, \varphi_2)$ on SO(3) around a preferred orientation $g_0 = g(\varphi_1^0, \theta^0, \varphi_2^0)$.

We consider Aluminium as example of polycrystal material with $s_{11} = 1.57$, $s_{12} = -0.57$ and $s_{44} = 3.51$ (all units: 10^{-11} Pa^{-1}) [8] and a rolling texture $(1,1,2)[\bar{1},\bar{1},1]$. The main representation matrix for this orientation is

$$\begin{pmatrix} -\frac{1}{\sqrt{3}} & \frac{1}{\sqrt{2}} & \frac{1}{\sqrt{6}} \\ -\frac{1}{\sqrt{3}} & -\frac{1}{\sqrt{2}} & \frac{1}{\sqrt{6}} \\ \frac{1}{\sqrt{3}} & 0 & \frac{\sqrt{2}}{\sqrt{3}} \end{pmatrix}. \tag{15}$$

The parameters $\bar{a}$ and $\bar{b}$ define the strength of the texture: smaller parameters indicate crystallites lying closer to the main orientation. Figure 2 allows the comparisson of the nutation angle dispersion corresponding to various $\bar{a}$ and $\bar{b}$ for the same given RTN texture. Obviously the dispersion

8

of Λ_{ij} and S_{ij} depends on the strength of the texture and increase with its decrease.

For further insight into the relation between $\bar{a}$ and $\bar{b}$ and the corresponding distributions of the various S_{ij} quantities we performed Monte Carlo simulations with 10000 realisations for several values of $(\bar{a}, \bar{b})$. The resulting S_{ij} distributions are shown in Figures 3 and 4.
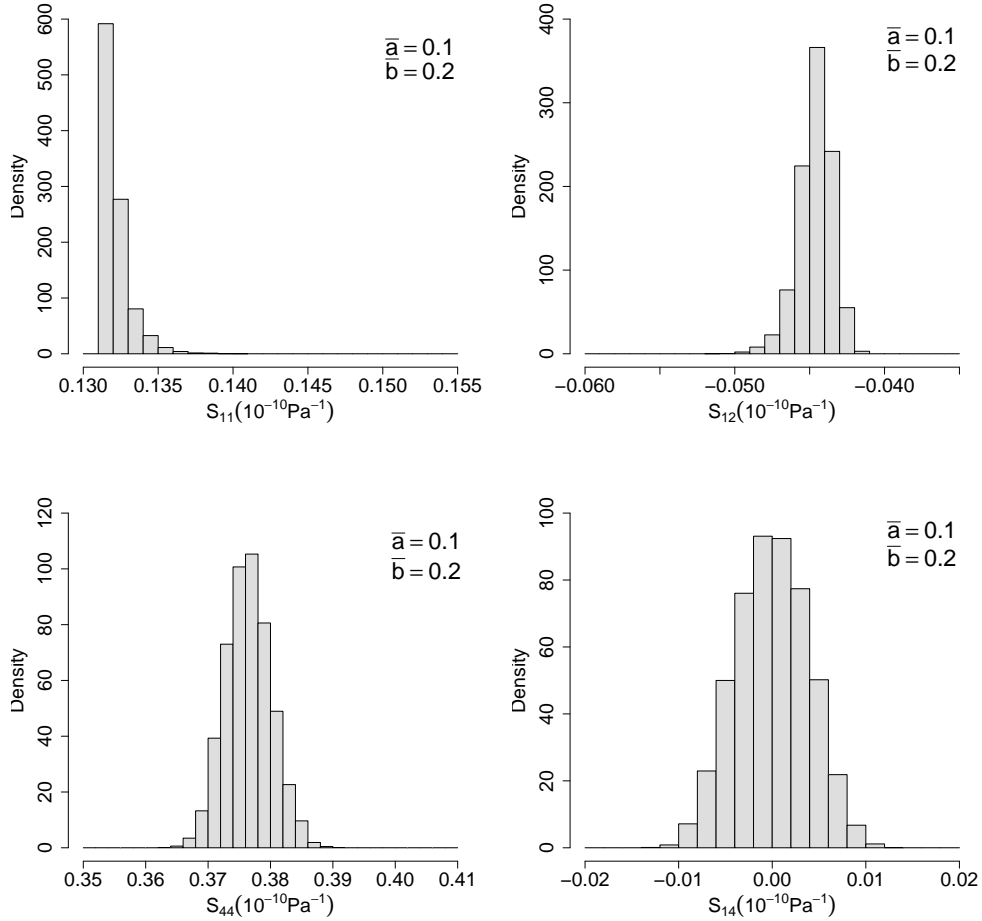
Figure 3: Distributions of various S_{ij} for $\bar{a} = 0.1$ und $\bar{b} = 0.2$.

Obviously, with increasing parameters $\bar{a}$ and $\bar{b}$ the set of small rotations $\Pi(a, b)$ increases to the full set $\{0 \leq \theta \leq \pi; \; -\pi \leq \varphi_1; \varphi_2 \leq \pi\}$ and the
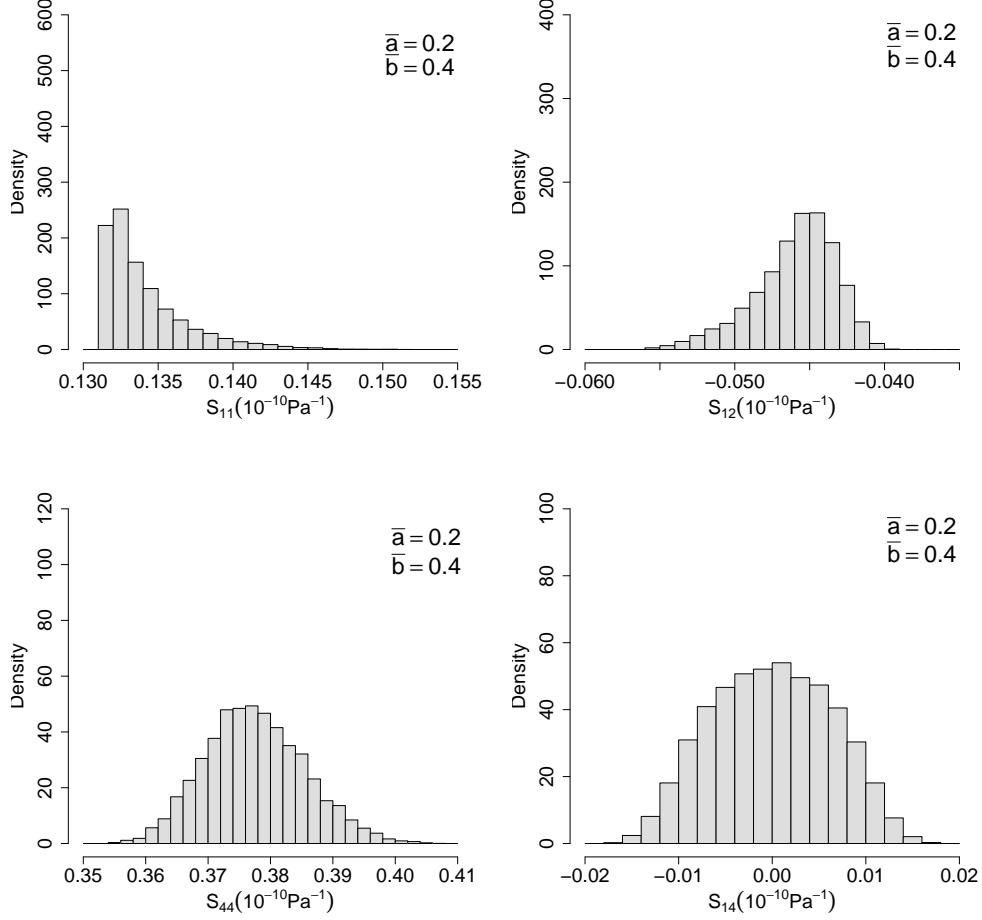
Figure 4: Distributions of various S_{ij} for $\bar{a} = 0.2$ und $\bar{b} = 0.4$.

distribution of orientations becomes a uniform distribution on SO(3).

Using the distributions of the elastic moduli we are able to derive the distributions of the Young's modulus in arbitrary directions $E_{\alpha\alpha}$, the Shear modulus $G_{\alpha\alpha}$ and the Poisson's ratio $\nu_{\alpha\alpha}$. As an example we have

$$E_{WW} = 1/S_{11} \quad , \quad G_{WQ} = 1/S_{44} \quad , \quad \nu_{WQ} = -S_{12}/S_{11}. \tag{16}$$

Figure 5 displays parameter distributions under two different textures, each obtained for $\bar{a} = 0.15$, $\bar{b} = 0.3$ and $n = 100$, based on 10000 Monte
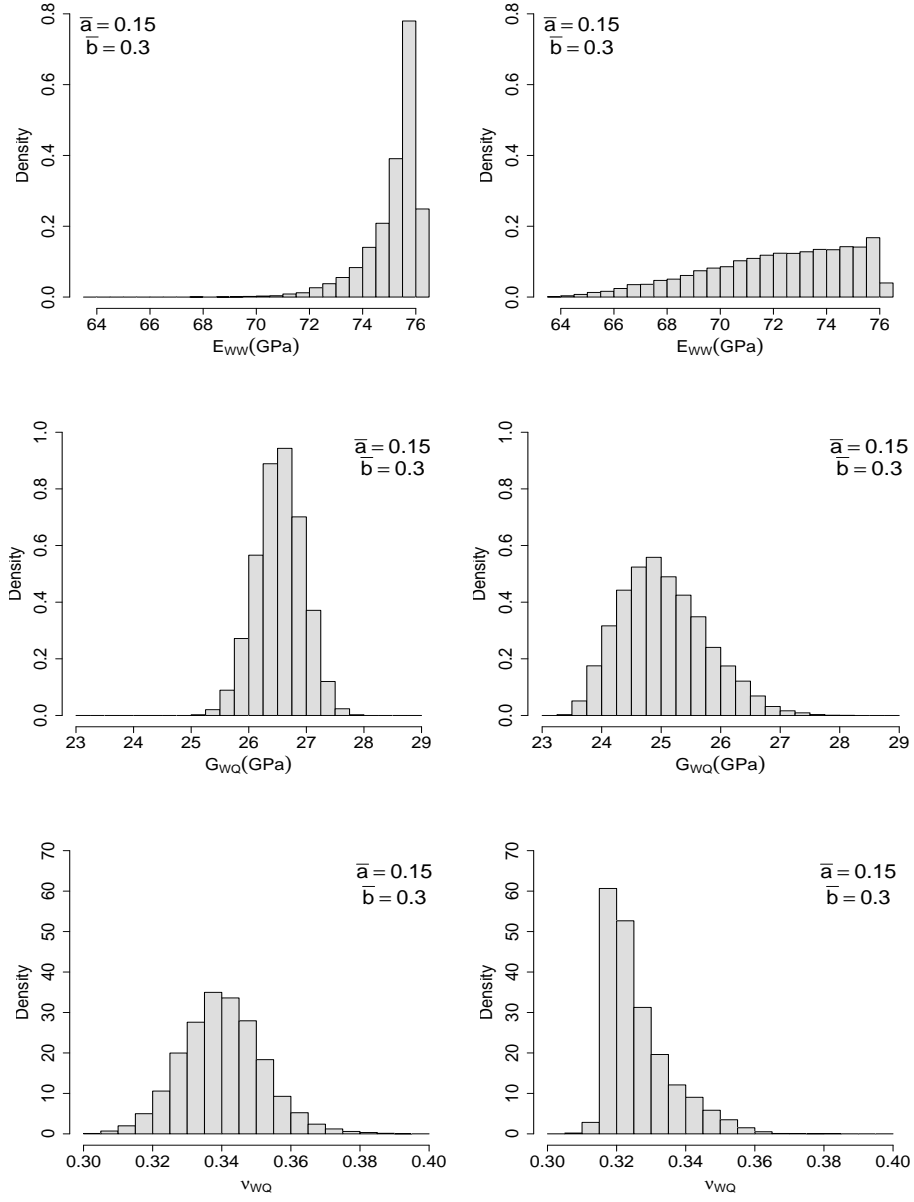
Figure 5: Histogram of the distribution of various elastic parameters for $\bar{a} = 0.15$, $\bar{b} = 0.3$, and $n = 100$. Left column: texture $(1,1,2)[\bar{1},\bar{1},1]$, right column: texture $(1,1,0)[1,\bar{1},2]$.
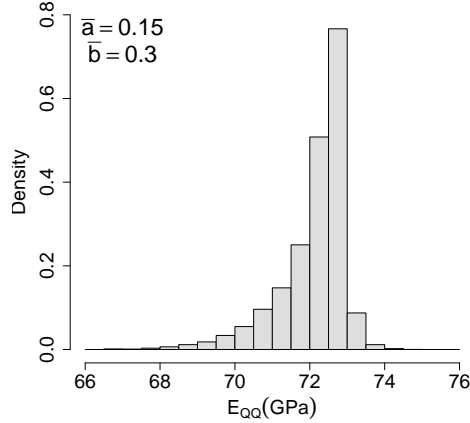
Figure 6: Histogram of the distribution of the distribution of the Young's modulus $E_{QQ} = 1/S_{22}$ for $\bar{a} = 0.15$, $\bar{b} = 0.3$ and $n = 100$.

Carlo realisations. Figures in the left column contain E_{WW}, G_{WQ} and ν_{WQ} for the texture $(1,1,2)[\bar{1},\bar{1},1]$ from above, while the right column of figures refers to the texture $(1,1,0)[1,\bar{1},2]$.

Having determined the distributions of interest by Monte Carlo simulation we can derive descriptive quantities for this distribution. As an example, we have for the Shear modulus in the left column of Figure 5 (all values in GPa)

Mean	SD	Min	Q1	Median	Q3	Max
26.54	0.40	25.08	26.27	26.54	26.81	27.87

Figure 6 displays the distribution of $E_{QQ} = 1/S_{22}$, again for the texture $(1,1,2)[\bar{1}, \bar{1}, 1]$.

The matrix entries S_{ij} are complicated functions of the Euler angles which cannot be described by simple standard distributions. However, we can obtain all characterizing quantities of these distributions up to a histogram or density estimate of the complete distribution in a relatively simple way. As additionally all distributions have compact support, an approximation by polynomials or mixtures of these may be considered.

For strongly textured material ($\bar{a} \leq 0.2$ and $\bar{b} \leq 0.3$) the distributions of some S_{ij} may well be approximated by normal or log-normal distributions. A more precise description of the S_{ij} distributions can be obtained by mix-

tures of distribution. This aspect, however, lies outside the scope of this contribution.

A further problem is the determination of the parameters q and r (corresponding to $\bar{a}$ and $\bar{b}$) of the canonical normal distribution (6) for a material measured experimentally. These can be derived from the pole figures [6].

3. Finite element simuations

3.1. Simulation strategy

The stochastic models from the previous section were used as inputs for a series of finite element simulations on RVEs. This makes possible the analysis of the different responses of an RVE under single mechanical loads. All the performed simulations use the resulting distributions from section 2, coresponding again to Aluminium with the texture $(1,1,2)[\bar{1},\bar{1},1]$.

From this texturized material, an RVE was defined as a cubic microcell of size equal to the thickness of the Aluminium foil under consideration, it is a cell of size 0.45mm × 0.45mm × 0.45mm.

In order to create a polycrystal inside this RVE, we take a number of randomly distributed points inside it and consider each of them as the center of one single crystal. The complete geometry insde the RVE is then partitioned using the Voronoi diagram of these centers. Finally, once the geometry of each single crystal is known, a thetrahedral mesh is constructed using the algorithms from [9].

With this, the resulting mesh has the property that every single thetrahedron belongs exclusively to one crystal in the RVE and the crystal boundaries are perfectly approximated by thetrahedral faces. Figure 7 shows three examples of this process, the upper row shows the Voronoi tesselations obtained for three different sets of random centers, while the lower row shows their corresponding meshes fitting to the geometry of the RVE.

Once the RVE's internal geometry has been meshed, the simulated elastic properties from Section 2 can be used in each single crystal. This is done by assigning one realisation of the 21 elastic constants of the stiffness matrix into each crystal, it is, one matrix for each mcrystallite inside the RVE.

The FEM simulation of the mechanical loads into a microcell is then performed by solving the elasticity problem

$$-\text{div}(\sigma) = f, \tag{17}$$

13
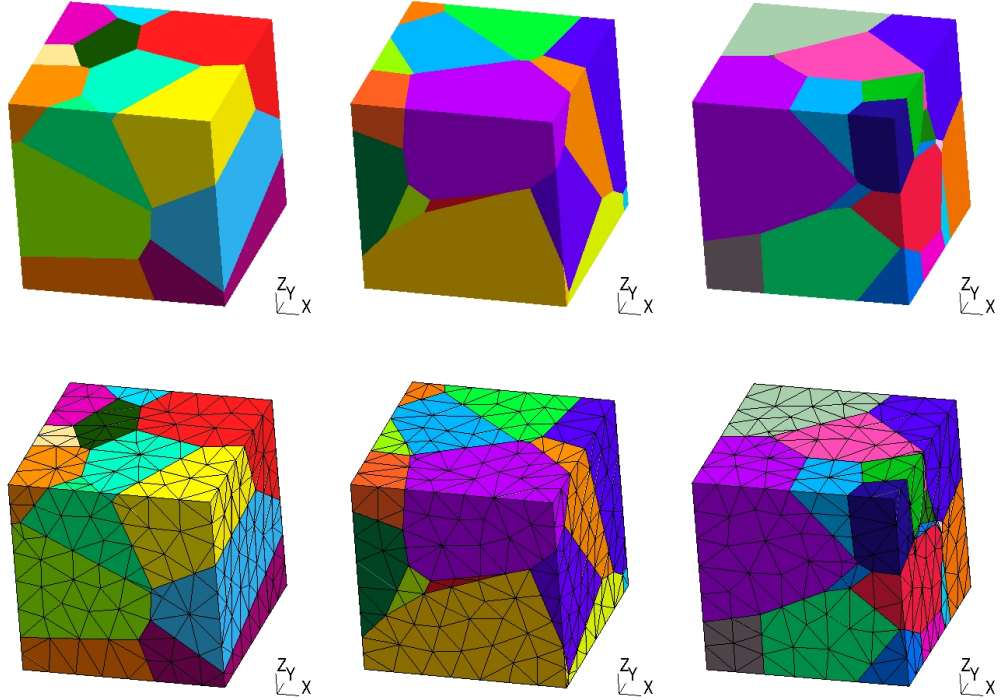
Figure 7: Examples of simulated microcells. The upper row shows Voronoi tesselations and the lower row shows their corrsponding meshes fitting to the geometry of the RVE.

with the tensors for stress and strain given as

$$\sigma(x) = C(x)\,\varepsilon(x), \tag{18}$$

$$\varepsilon(x) = \frac{1}{2}\left(\nabla u(x) + \nabla u(x)^T\right), \tag{19}$$

respectively, and with u denoting the deformation as fuction of the position x.

All the FEM simulations were performed using an anisotropic implementation for the elasticity problem in the Toolbox ALBERTA [10], which is based on the previously existent isotropic implementation of the elastic solver.

It is important to note that the resulting system to solve the elasticity problem must be able to handle the full local anisotropies in each crystal (given by a full stiffness matrix C in every point of the cell) as well as the

14

different values of the elastic properties existent among the different crystals conforming the RVE. At this point, the correct construction of a mesh fitting the monocrystal boundaries becomes important, as there is no thetrahedra having quadrature points belonging to different crystals.

3.2. Responses of an RVE for the different deformation modes
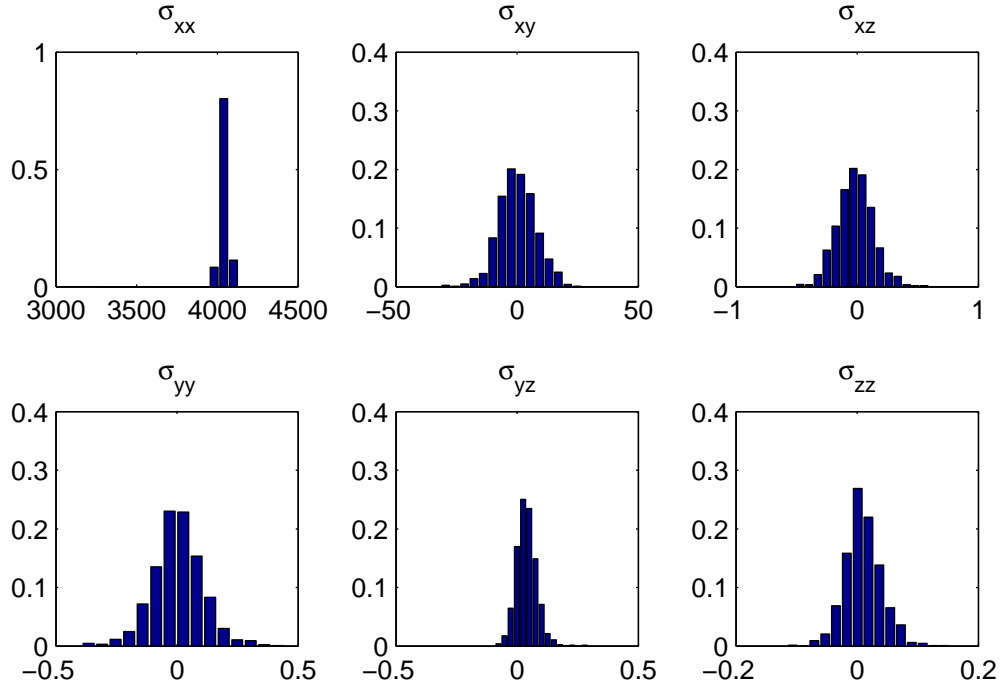
Figure 8: Distributions of volume averaged stresses [Pa] in the microcell under an applied strain of $\varepsilon_{xx} = 0.01$.

To analyse the microcell's responses to a given mechanical load, we perform a single mode analysis in which the cell is only affected by a mechanical strain with one component diferent from zero, it is

$$\varepsilon = \gamma e_i, \tag{20}$$

where e_i denotes a unitary vector in $\mathbb{R}^6$.

The value of the factor γ represents the amount of strain applied in the corresponding component and, for the simulations performed here was taken

15
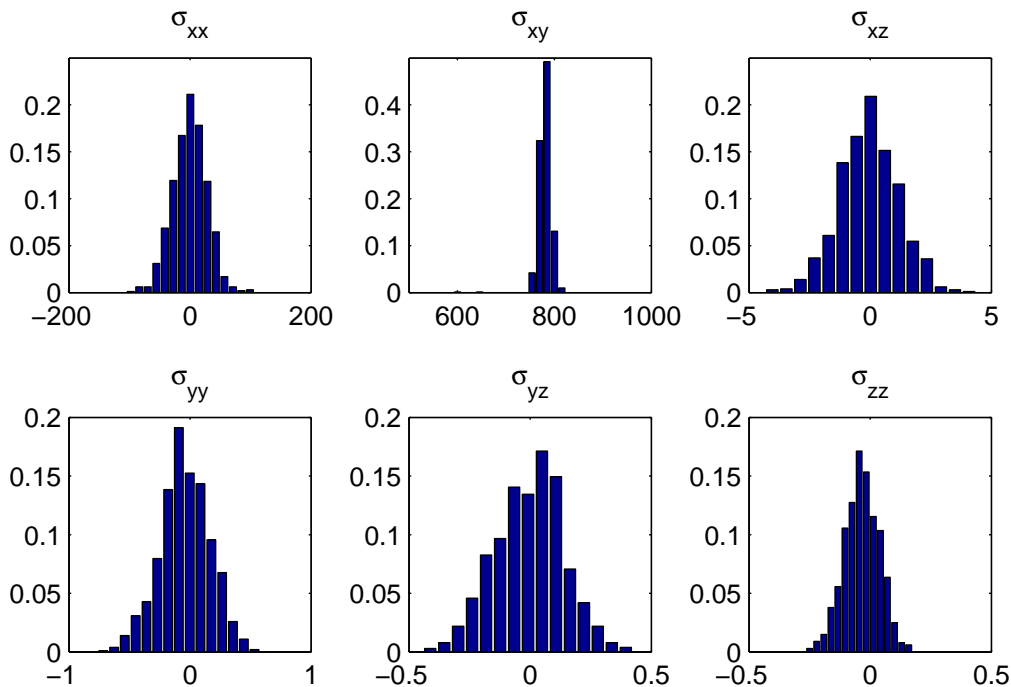
Figure 9: Distributions of volume averaged stresses [Pa] in the microcell under an applied strain of $\varepsilon_{xy} = 0.01$.

as 0.01, (this means that the cell is strained by 1%). The actual problem solved for this analysis considers a right hand side $f = 0$ and boundary conditions of Dirichlet type for the inclusion of the strain in equation (20). For example, for including a shear strain of size γ in the xy-plane, the boundary conditions for the deformation look like

$$u(x) = \begin{pmatrix} 0 & \gamma & 0 \\ \gamma & 0 & 0 \\ 0 & 0 & 0 \end{pmatrix} x, \qquad (21)$$

for all points $x \in \mathbb{R}$ belonging to the microcell's boundary.

Such boundary conditions result in an elongation of the microcell's geometry in the cases where γ appears as diagonal entry of the matrix. In case γ appears in the off-diagonal elements of the matrix, as in equation (21), the microcell will present a shear in the ij-plane.

With this ideas, we can decompose every strain affecting a microcell as

16
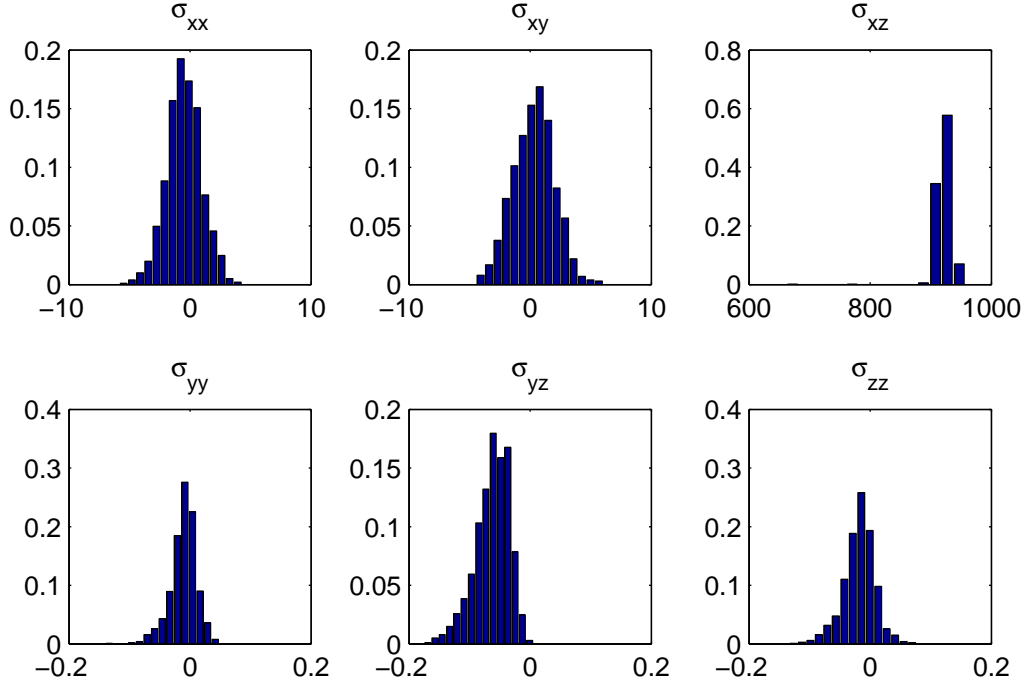
Figure 10: Distributions of volume averaged stresses [Pa] in the microcell under an applied strain of $\varepsilon_{xz} = 0.01$.

the sum of the 6 components of strain and, in the case of linear elasticity, the resulting stress can be easily computed as the sum of the corrsponding elastic stresses for each component.

The stochastic response of a microcell was computed using a number of 1000 FEM simulations for each of the strain modes. Each of the simulations was performed using the same procedure for the creation of the microcell's geometry, its voronoi tesselation, the mesh and the assignment of local elastic properties of every single crystal.

The results of the 1% strain applied to the RVE in each of the modus are presented in Figures 8–13 as histograms of the resulting stress values. The horizontal axis represents the value of the stress component and the vertical one is the probability density of obtaining this value. The presented values for the stress correspond to the volume averaged values over the three
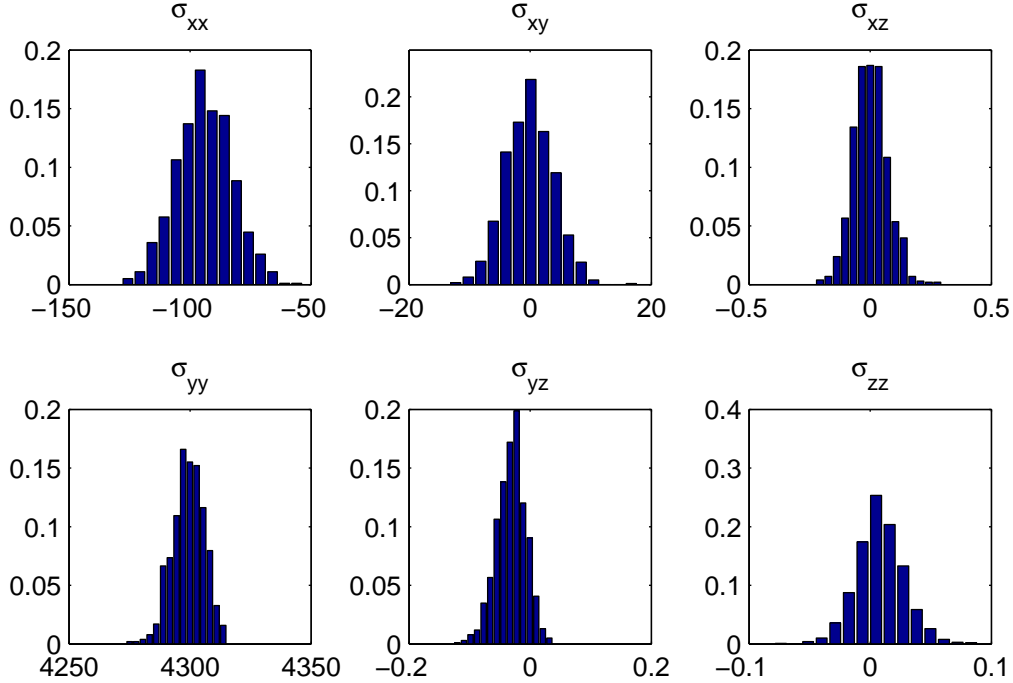
Figure 11: Distributions of volume averaged stresses [Pa] in the microcell under an applied strain of $\varepsilon_{yy} = 0.01$.

dimensional microcell, it is

$$\bar{\sigma}_{ij} = \frac{1}{V} \int_{\Omega} \sigma_{ij}, \tag{22}$$

where V denotes the volume and $\Omega \subset \mathbb{R}^3$ represents the RVE's domain.

Figure 8 shows the resulting distributions for an elongation of the microcell in the x direction. In this figure, it can be observed how the xx-component of stress results in the highest values in the order of 10^3, while almost all other components are on the order of 10^{-1}, with the only exception on the xy component. The higher values in the xy component are an interesting feature that indicates that the material presents strong connections between the mechanical responses in the x and y directions.

Figures 11 and 13 show the corresponding responses for the elongation modes in the y and in the z direction, repeating the general result of having the largest values in the yy and the zz components, respectively. Figure 11

18
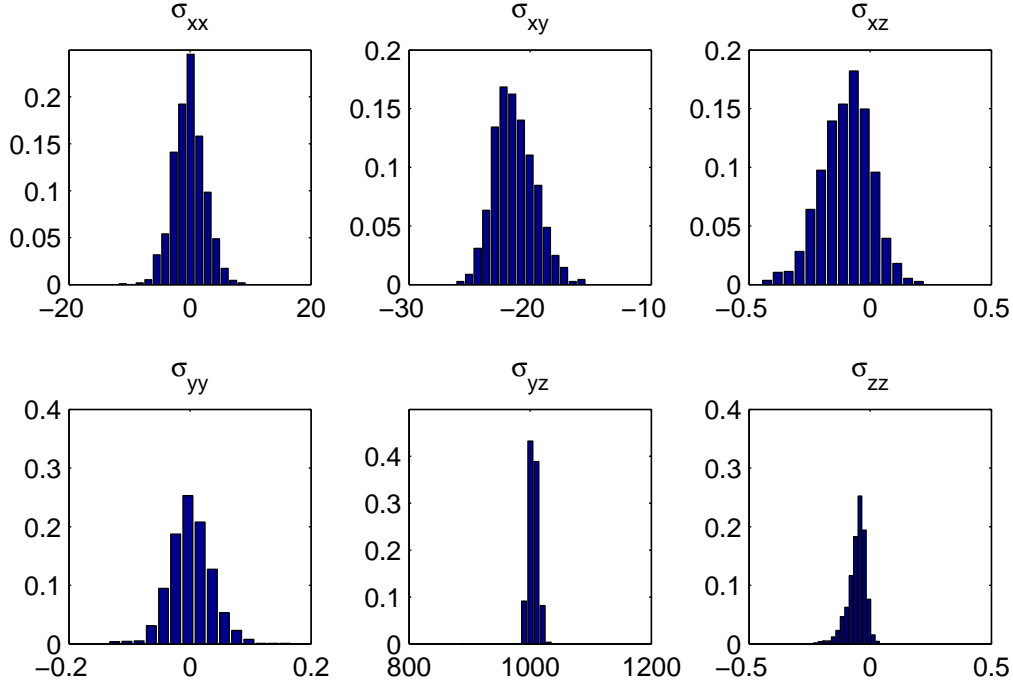
Figure 12: Distributions of volume averaged stresses [Pa] in the microcell under an applied strain of $\varepsilon_{yz} = 0.01$.

confirms the close relation between the x and y directions, with the xx and the xy components having the largest volume averaged stress values (after the yy component itself).

Note that although the applied strain was of 1% in all cases, for the shear modes xy, xz and yz there are much lower values in the responses. All the values are about one order lower that the maximum values obtained for the tensile modes xx, yy, and zz.

It is interesting to observe that the obtained distributions cannot be assumed to be of the same kind, even for the same component of the stress tensor. Example of this are the components yz of each response (fifth subplots in Figures 8–13).

As already mentioned before, we claim that the complete response of the material behavior can be modelled as sum of the six modes presented here. Thus, the stress responses of the material correspond to a weighted sum of modal distributions, which makes the complete-response distributions far
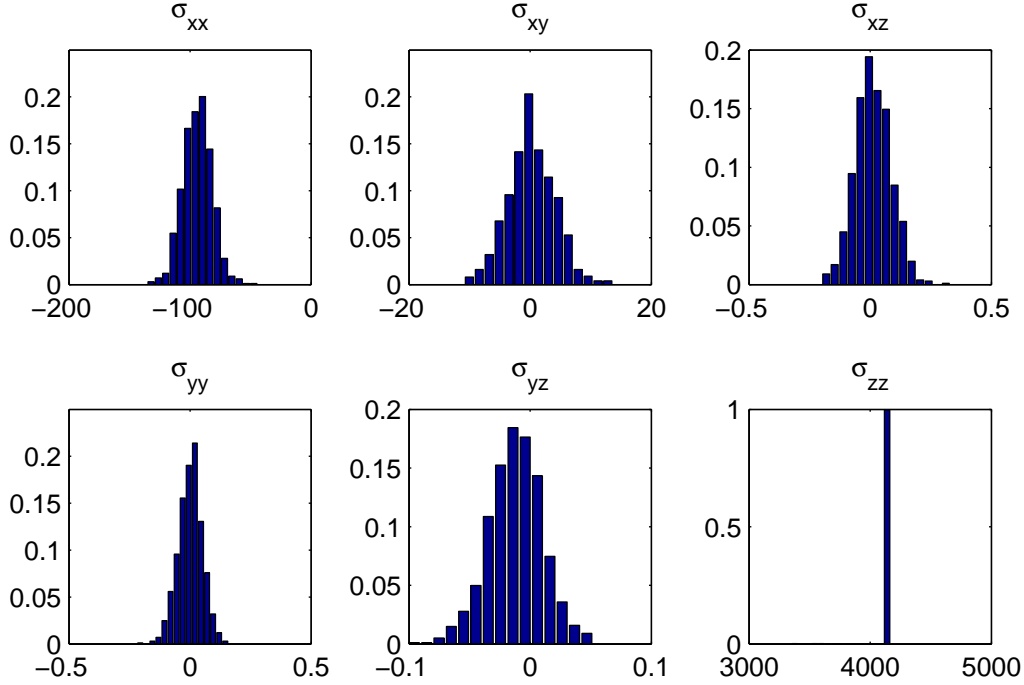
Figure 13: Distributions of volume averaged stresses [Pa] in the microcell under an applied strain of $\varepsilon_{zz} = 0.01$.

from being trivial, specially for texturized materials.

4. Conclusion and future works

The methods presented here are an effective way of calculating the mechanical responses of texturized materials under given loads, including the uncertainities of the single crystal orientations and the anisotropies from the polycrystals' stochastic geometry.

From the stochastic models in Section 2, it is worth to mention that they can also be used for the calculation of further material parameters that allow representation by tensor quantities.

Although these models are useful for the simulation of many effects in polycrystals, it must be noticed that they were obtained without considering the possible correlations between properties of different crystallites. Includ-
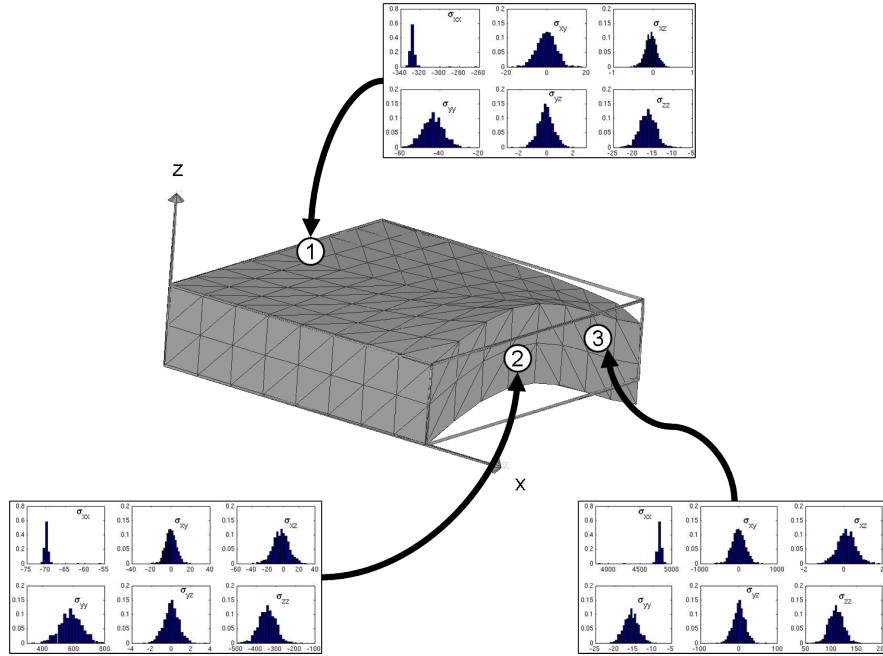
Figure 14: Small plate computed with the expectation values and three stress responses.

ing such correlations into the consideration will become important while trying to analyse multiphase polycrystals and will be part of our future works.

The mechanical responses in form of probability densities can be used as part of a two-scale method similar to the ones presented in [11, 12]. For these methods, the solution of the mechanical problem in a complete piece requires the solution of micro-problems on RVEs for each quadrature point of the macroscale mesh (often on the order of thousands). Using the distributions to calculate the stress effect for given strains would avoid the expensive computation of all the microcell problems and derive in a much faster two-scale simulation, where the microscale already contains the uncertainities and anisotropies of the texture.

Another possibility is to use the stiffness tensor's expectation to compute the macroscale simulation. Using the results for this simulation, the values of strain can be taken as inputs of the microscale response and the uncertainty belonging to each quadrature point on the macroscale can be easily assigned.

Following this last idea, Figure 14 shows the computed deformation on a

$\varepsilon_{xx} = -0.000812, \quad \varepsilon_{xy} = 0.001713 \quad \varepsilon_{xz} = 0.000986, \quad \varepsilon_{yy} = 0.004629, \quad \varepsilon_{yz} = 0.002299, \quad \varepsilon_{zz} = 0.001732$
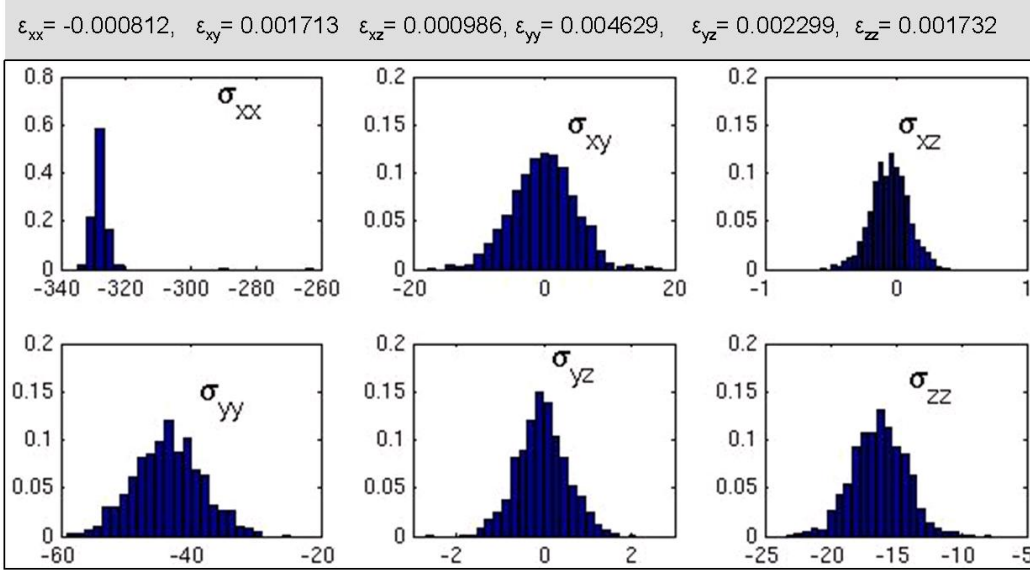
Figure 15: Stress response distributions obtained for one of the points shown in Figure 14. Point 1: (0.1875, 1.1875, 0.3750).

small plate of size 2.0mm × 2.0mm × 0.5mm in which the sides corresponding to the planes $x = 0$ and $y = 0$ were fixed, while the boundary corresponding to the plane $x = 2$ were artificially set as

$$u(x, y, z) = \begin{pmatrix} 0 \\ 0 \\ \sin(2y) \end{pmatrix}. \tag{23}$$

The responses at three different points are also schematically shown in Figure 14, and the detailed values of this points are included in the corresponding Figures 15, 16, and 17. Here is important to recall the fact that for an already known set of mechanical responses, the computational costs for obtaining th values shown in Figures 15–17 are practically the same as the costs of the macroscale computation alone.

Regarding the inclusion of the stochastic models for the polycrystal constitution into the FEM simulations, both the two-scale computation and the local response strategies will be followed in our future research.
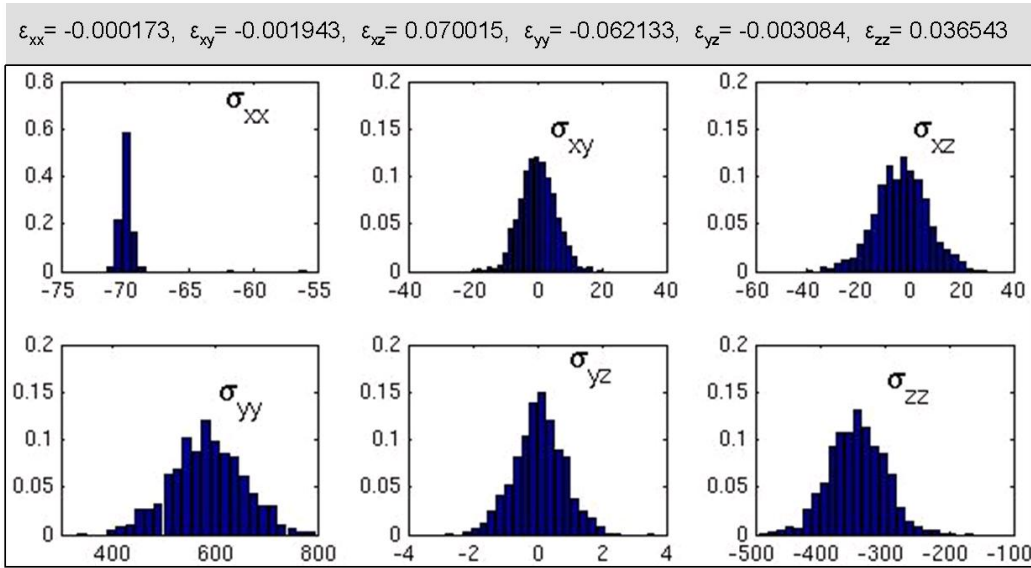
Figure 16: Stress response distributions obtained for one of the points shown in Figure 14. Point 2: (1.8125, 0.9375, 0.1250).

Acknowledgements

References

[1] H.-J. Bunge, Mathematische Methoden der Texturanalyse, akademie Verlag Berlin, 1969.

[2] P. Bobrov, J. Montalvo-Urquizo, A. Schmidt, W. Wosniok, Mechanic-stochastic model for the simulation of polycrystals, submitted to ZAMM Journal of Applied Mathematics and Mechanics (2010).

[3] A. Wiglin, Quantitative description of textures for polycrystal material, Physics of the Solid State 2 (1960) 2463 – 2476.
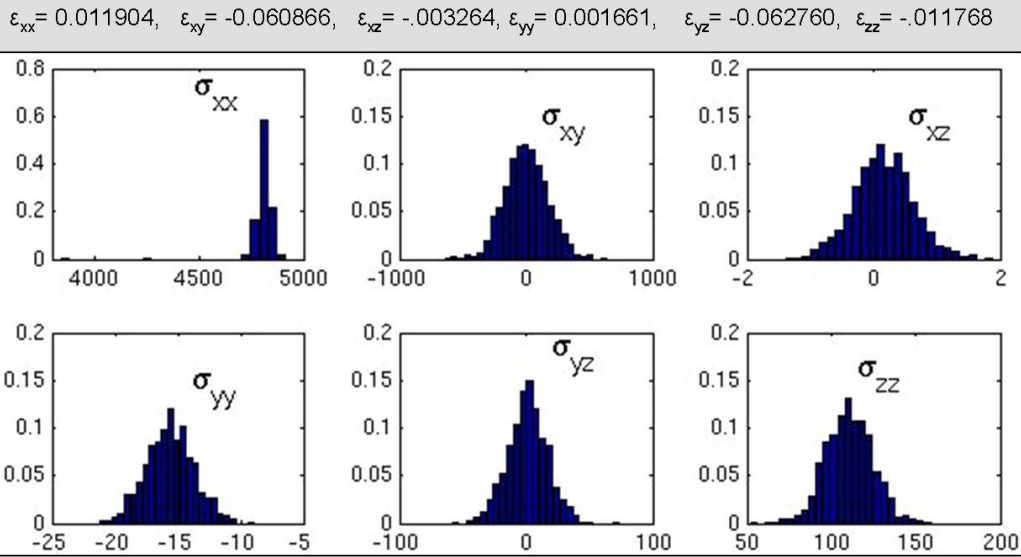
Figure 17: Stress response distributions obtained for one of the points shown in Figure 14. Point 3: (1.8125, 0.9375, 0.1250).

[4] T. Savyolova, Distribution functions of grains with respect to orientation in polycrystals and their Gaussian approximations, Industrial Laboratory 50 (1984) 468 – 474.

[5] K. Parthasarathy, The central limit theorem for the rotation group, Theory of Probabilities and its Application 9 (1964) 273 – 282.

[6] T. Savyolova, Approximation of the pole figures and the orientation of distribution of grains in polycrystalline samples by means of canonical normal distributions, Textures and Microstructures 22 (1993) 17 – 27.

[7] M. Borovkov, T. Savyolova, Approximation of the class of canonical normal distributions by means of the method of random rotations in the texture analysis., Industrial Laboratory 68 (2002) 16 – 21.

[8] I. Francevič, F. Voronov, S. Bakuta, Elasticity constants and elastic moduli of metallic and non-metallic materials (in Russian), Naukova Dumka, Kiev, 1982.

24

[9] R. Quey, Neper: a software to build 3D random polycrystals for the finite element method (version 1.8.1), http://neper.sourceforge.net (2009).

[10] A. Schmidt, K. G. Siebert, Design of Adaptive Finite Element Software: The Finite Element Toolbox ALBERTA, Springer, 2005.

[11] F. Feyel, J.-L. Chaboche, FE^2 multiscale approach for modelling the elastoviscoplastic behaviour of long fibre SiC/Ti composite materials, Comput. Methods Appl. Mech. Engrg. 183 (2000) 309 – 330.

[12] V. Kouznetsova, Computational homogenization for the multi-scale analysis of multi-phase materials, Ph.D. thesis, TU Eindhoven (2002).